



Atomically dispersed Sn modified with trace sulfur species derived from organosulfide complex for electroreduction of CO₂

Xin Wang^{a,*}, Fengli Li^{b,1}, Wen-Jin Yin^{c,1}, Yubing Si^a, Ming Miao^a, Xiaoming Wang^a, Yongzhu Fu^{a,*}

^a College of Chemistry, Zhengzhou University, Zhengzhou 450001, PR China

^b College of Chemistry, Chemical Engineering and Materials Science, Zaozhuang University, Zaozhuang 277160, PR China

^c School of Physics and Electronic Science, Hunan University of Science and Technology, Xiangtan 411201, PR China

ARTICLE INFO

Keywords:

Tin
Bis(benzene-1,2-dithiolato) complex
Sulfur species dopant
CO₂ electroreduction
Structure-activity relationship

ABSTRACT

Electrochemical CO₂ conversion into fuels is highly desirable to achieve carbon artificial cycles. Among electrocatalyst candidates, earth-abundant tin is subject to unsatisfied efficiency and selectivity. In this work, atomically-dispersed Sn nanoclusters modified with the trace of sulfur doping are proposed to efficiently electroreduce CO₂ to C₁ chemicals. This electrocatalyst is in situ derived from bis(benzene-1,2-dithiolato). It exhibits a high Faradaic efficiency (90%) for carbonaceous products at a moderate overpotential (0.75 V). Importantly, it is exploited for the formate formation with unprecedented partial current density (90 mA cm⁻²) and long-term stability (50 h) using the flow cell, better than most Sn-based catalysts. Electrochemical experiments and theoretical calculations manifest the promoting effect of trace sulfur on Sn nanoclusters, which stabilizes the *HCOOH intermediate and favors CO₂ electroreduction. Hence, it emphasizes the importance of dopants and charge modulating for performance enhancement. This work unfolds a promising candidate for Sn electrocatalysts towards CO₂ electroreduction.

1. Introduction

The excessive utilization of fossil fuels has provoked the increasing atmospheric CO₂ concentration, triggering tremendous climatic disasters and perturbations to natural ecosystems [1,2]. To address these issues, the conversion of CO₂ into chemical feedstocks powered by the renewable energy is considered as a promising solution [3–5]. Technologies for CO₂ electrochemical reduction reaction (CO₂RR) have the potential to close the anthropogenic carbon cycle, and transfer CO₂ into value-added products [6,7]. Nevertheless, an efficient and cost-effective synthetic scheme for CO₂RR is far from trivial due to its thermodynamically stable nature [8]. Among the various sub-product options, formate (or formic acid), has been receiving great attention because of its utilization in fuel cells [9–11] and considerable economic value (1000 € per metric ton). Recently, many works have reported the formate production using metal catalysts with high electronic conductivity and considerable activities [12,13]. For example, main group metals (In [14], Sn [15], Pb [16], and Bi [17,18]) favor the formate

generation because of their high H₂ evolution overpotential and weak CO adsorption. Considering the investment costs, inexpensive and robust electrocatalysts with high efficiency are significantly worthy for further CO₂RR. Therefore, Sn-based catalysts emerge themselves for the formate formation due to their low-cost, low-toxicity, and environmental friendliness.

Although there are numerous reports dealing with tin electrodes for CO₂RR, their practical applications are greatly impeded by the low efficiency and high overpotential [19]. Therefore, many strategies have been developed to enhance Faraday efficiency (FE) and current density, such as atomically dispersion engineering [20–22], morphology engineering [23], defect engineering [24], and surface functionalization engineering [25]. For example, Kanan's group confirmed that oxide-derived metals (such as Au, Cu, Pd, and Sn) exhibited better activity, higher selectivity, and longer durability compared to the pure metal [11–13]. And even the tin electrocatalyst under reducing potentials is still covered with metastable SnO_x and the catalytic active site is the Sn(II) oxyhydroxide observed by the in situ attenuated total

* Corresponding authors.

E-mail addresses: wangxin0620@zzu.edu.cn (X. Wang), yfu@zzu.edu.cn (Y. Fu).

¹ Xin Wang, Fengli Li, and Wen-Jin Yin contributed equally to this work.

reflectance infrared spectroscopy [9]. Based on these previous studies, the local environment of metal, especially dopants or adatoms, is expected to enhance the selectivity due to the charge density redistribution of reaction sites. Besides the oxide-derived Sn, catalysts derived from other sources are still waiting to be developed. Chalcogenides have demonstrated their potential towards CO₂RR, such as MoS_x [26], Sn/SnS₂ [27], Ni-doped SnS₂ [28], SnS [29], and S-modulated Sn [30]. Despite these works, the key species for Sn catalysts have not been identified, and it is unknown the contribution of surface dopants to the catalytic behavior. As such, developing sulfide-derived Sn with the abundant doping toward desirable products is imperative for both fundamental research and practical application.

In this work, we modified atomically Sn nanoclusters with trace of sulfur doping (denoted as Sn NCs:S) derived from a metal-organosulfide complex (1,2-Sn(BDT)₂). This Sn NCs:S catalyst exhibits higher current density (42 mA cm⁻² at -1.1 V_{RHE}) and Faradaic efficiency (90%) for carbonaceous products than Sn nanoparticles and SnS₂ nanosheets. Compared with homologous Sn-based catalysts, it possesses a astonishing formate partial current density (35 mA cm⁻²) at a moderate overpotential (0.88 V). Moreover, we apply Sn NCs:S in a flow cell, which represents industry-desirable current density (200 mA cm⁻² at -1.1 V_{RHE}), low overpotential (700 mV for achieving 80% FE_{formate}), and robust lifetime of over 50 h. More importantly, it is observed the effect of trace sulfur in promoting CO₂RR for Sn-based catalysts according to the electrochemical experiment and impedance analysis. Theoretical calculations reveal that the trace of sulfur doping facilitates the second protonation and stabilizes the *HCOOH intermediate. This work develops the Sn-based catalyst from the organosulfide complex with unprecedented performance for CO₂RR and uncovers the potential mechanism of the trace sulfur doping with the improved catalytic activity.

2. Experimental section

2.1. Chemicals

1,2-benzenedithiol (C₆H₆S₂, 1,2-BDT), SnCl₄, Sn nanopowder, and SnS₂ were purchased from Alfa Aesar. D₂O, 3-(Trimethylsilyl)-1-propanesulfonic acid sodium (DSS), ethanol (absolute GR, 99.7%), and HCOOH (> 99.99%) were purchased from Macklin. Super P was purchased from Guangdong Canrd New Energy Technology Co., Ltd. Nafion perfluorinated ion-exchange resin solution (5 wt.% in mixture of alcohol & H₂O) was purchased from Sigma Aldrich. Nafion® N-117 membrane was purchased from Alfa Aesar. Carbon fiber paper (CP) was obtained from FuelCell. All the chemicals were used without further purification.

2.2. Synthesis of the catalysts

2.2.1. Preparation of Sn-(BDT)₂ NR

1,2-BDT and SnCl₄ were dissolved in ethanol and water, respectively. Then, 1,2-BDT solution was added into the SnCl₄ solution drop by drop in a molar ratio of 2:1 under an ice bath. Once two reactants encountered, the red compound was immediately formed and suspended in the solution. The turbid liquid was stirred for 5 h followed by keeping in the refrigerator for 12 h, washing, and freeze drying. Finally, red solid sample was collected.

2.2.2. Electroreduction of Sn NCs:S

Sn-(BDT)₂ (5 mg) and Super P (1 mg) were dispersed in 1 mL of ethanol with the addition of 100 μL of 5 wt.% Nafion, and sonicated for 40 min as slurry. The slurries of commercial Sn, SnS₂, and Super P were prepared using the same procedure. The slurry was drop-casted onto a 1 × 1 cm² Teflon-treated carbon fiber paper (HCP020P, from HESN AvCarb P75) to reach areal loading of 1 mg cm⁻² and naturally dried. Electroreductions were performed in a custom-designed gas-tight H-shaped electrochemical cell with two compartments separated by a

Nafion-117 membrane. CP modified with catalysts and saturated Ag/AgCl electrode were used as the working and reference electrode and placed in the cathodic compartment. A graphite rod was used as the counter electrode and placed in the anodic compartment. Each compartment contained 30 mL electrolyte (0.5 M KHCO₃), leaving a headspace of 25 mL. All the potential readings were iR-corrected, and converted to the RHE scale ($E_{RHE} = E_{Ag/AgCl} + 0.1981 \text{ V} + 0.0591 \text{ V} \times \text{pH} - i \times R \times 0.85$), and R is obtained from electrochemical impedance spectrum (EIS) data. Cyclic voltammetry (CV) test was performed at 10 mV s⁻¹ controlled by CHI 660E potentiostat. During the electroreduction, the working electrode was biased at -1.4 V_{Ag/AgCl} for 2 h. It was then quickly taken out from the electrolyte, and rinsed with deionized water for further characterizations. In contrast, the working electrodes of Sn nanoparticles, Super P, and SnS₂ were prepared under similar conditions with the same loading mass.

2.3. Electrochemical measurements

2.3.1. CO₂RR measurements using H-cell configuration

The H-cell configuration was the same as the above experiment. The electrolyte was pre-saturated with N₂ (pH = 8.4) or CO₂ (pH = 7.5), as shown in Fig. S1. For CO₂RR electrocatalysis on different electrocatalysts, CO₂ or N₂ gas (flow rate: 20 sccm) was continuously bubbled into the electrolyte. CV and polarization curves were carried out at 50 mV s⁻¹ and 10 mV s⁻¹, respectively.

2.3.2. Flow cell measurements

It was performed in a custom-designed flow cell reactor made of polytetrafluoroethylene plastic. It consists of two parts, which is Sn NCs:S loading gas diffusion electrode (GDE, 1.0 mg cm⁻², 1.5 × 3.5 cm²) as the cathode, a GDE-loading 20 wt.% Ir/C (same loading mass) as the anode and a piece of anion exchange membrane (SELEMION, 1.5 × 3.5 cm²) as the separator. The cathode and anode compartments are 4 cm³ each in volume. Ag/AgCl electrode was located inside the cathode compartment. During the measurements, CO₂ was directly fed to the cathode at a rate of 80 sccm. The catholyte was 1 M KOH and circulated at a rate of 10 sccm.

2.3.3. Product analysis

During the electrolysis, the gas products from the cathode compartment were continuously vented into a gas chromatograph (GC, PANNA A91PLUS) equipped with a packed bed column (HaySep D) operated at 80 °C with a thermal conductivity detector (TCD) and a flame ionization detector (FID). Argon was employed as carrier gas under 30 mL min⁻¹. The gaseous products were separated in a molecular sieve column (Alltech, part no. 57732, 3.0 m × 1/8 in., molecular sieve 13X, 60/80 mesh) and hydrocarbons in a HaySep column (Alltech, part no. 14487, 2.0 m × 1/8 in., HaySep Q, 80/100 mesh). The concentration of H₂ and CO was quantified by the integral area ratio of the reduction products to standards. Their Faradaic efficiencies were calculated as below:

$$FE_{\text{gaseous product}}(\%) = \frac{Q_{\text{CO or H}_2}}{Q_{\text{total}}} \times 100\% = \frac{\left(\frac{v}{s/\text{min}}\right) \times \left(\frac{24000}{\text{cm}^3/\text{mol}}\right) \times N \times F}{j} \times 100\% \quad (1)$$

where v (=20 sccm) is the flow rate of CO₂, x is the measured concentration of product in 0.5 mL sample loop based on the calibration of the GC with a standard gas, N (=2) is the number of electrons required to form a molecule of CO or H₂, F is the Faraday constant (96,500 C mol⁻¹), and j is the recorded current.

The liquid products were collected for each electrocatalysis and analyzed by ¹H nuclear magnetic resonance (NMR, Bruker AVIII HD 600). 0.5 mL of the catholyte was mixed with 0.1 mL of D₂O and 0.2 mL of DSS as the internal standard. The concentrations of formate was

quantitatively determined from their NMR peak areas relative to the internal standard using the calibration curve from HCOONa solutions. The Faradaic efficiency was calculated as follows:

$$FE_{\text{liquid product}}(\%) = \frac{Q_{\text{HCOO}^-}}{Q_{\text{total}}} \times 100\% = \frac{n_{\text{HCOO}^-} \times N \times F}{j \times t} \times 100\% \quad (2)$$

where n_{HCOO^-} is the measured amount of formate, N (=2) is the number of electrons required to form a molecule of HCOO^- , F is the Faraday constant (96,500 C mol⁻¹), t is the reaction time, and j is the recorded current. Reaction time for liquid product detection was chosen 10–15 min, which is general procedure in the literatures. Partial current density of formate was calculated by multiplying the overall current density and their corresponding Faradaic efficiency.

2.3.4. Electrochemically active surface areas (ECSA) measurement

The ECSA of the catalyst was calculated from the double-layer capacitance according to the reported literature [31].

$$\text{ECSA} = R_f \times S \quad (3)$$

where S was the geometric area of CP electrode (1.0 cm²) and R_f was the roughness factor calculated from the ratio of the double-layer capacitance (C_{dl}) for the working electrode and the CP electrode.

$$R_f = \frac{C_{\text{dl}}}{C_s} \quad (4)$$

where C_{dl} was a half of the slope of plots for the difference of anodic and cathodic current density ($\Delta j = j_a - j_c$) against scan rates in the non-faradic region. C_s was measured by a similar method without the catalyst.

2.3.5. Kinetic characterization

Tafel analysis is an efficient approach to obtain further mechanistic insight of the catalytic process. Generally, it is based on the polarization curve and Tafel equation ($\eta = a + b \times \log j$). EIS measurement was performed at the open circuit voltage with the frequency range from 1 MHz to 100 mHz and amplitude of 5 mV. The EIS analysis of Sn-based materials were carried out under the same conditions as the catalytic tests. Adsorption affinity of OH^- as a surrogate ion was examined by oxidative linear sweep voltammetry (LSV) scans from -0.2 to 0.5 V_{RHE} at 10 mV s⁻¹ in a two-compartment reactor filled with a N₂-bubbled 1 M KOH electrolyte [10].

2.4. Theoretical calculation

2.4.1. Computational method

The calculations were carried out by DFT in the Vienna ab initio simulation program package (VASP). Perdew-Burke-Ernzerhof (PBE) functional was used to describe the exchange-correlation term based on the generalized gradient approximation (GGA). The projector augmented wave (PAW) method was used to represent the atomic cores. The energy cutoff was set at 600 eV for the plane-wave basis, which yields total energies converged at least 0.001 eV per atom. The convergence criterion of the self-consistency process was set to 10⁻⁵ eV between two electronic steps. The Brillouin zone was sampled by the Monk-horst Pack scheme with a Γ -centered grid of $4 \times 4 \times 1$ k points for the supercell. The structures were fully relaxed until the residual force is less than 0.001 eV/Å on each atom.

In the text, we adopted three typical structures to model including Sn (200) slab, S-doped Sn (200) slab, and monolayer SnS₂ sheet. As for the Sn (200) case, a (2 × 3) supercell was used, while a (3 × 3) supercell is used for the SnS₂ sheet. The adsorbability of molecular CO₂ and its intermediate states on substrates were checked by the adsorption energy, which is expressed by:

$$\Delta E = E_{\text{sub+mol}} - E_{\text{sub}} - E_{\text{mol}} \quad (5)$$

where $E_{\text{sub+mol}}$ and E_{sub} are the total energy of the substrate with and without molecule adsorbed on the substrates, and E_{mol} is the energy of the free molecule in vacuum. Within the computational hydrogen electrode (CHE) model, the chemical potential of a proton-electron pair is equal to that of half a H₂ molecule. Furthermore, to know the thermodynamic behavior of CO₂RR, the Gibbs free energy for each elementary step is calculated as:

$$\Delta G = \Delta E_{\text{DFT}} + \Delta \text{ZPE} - T\Delta S \quad (6)$$

where ΔE_{DFT} , ΔZPE , and ΔS are the differences in DFT total energy, zero-point energy and entropy of the two states before and after reaction, respectively; temperature T is set to 298 K. Standard ideal gas methods were employed to compute E_{ZPE} and TS from temperature, pressure, and the calculated vibrational energies. For adsorbate, all 3 N degrees of freedom were treated as frustrated harmonic vibrations with negligible contributions from the catalysts' surfaces.

3. Results and discussion

3.1. Synthesis and characterization of Sn-BDT nanorods (NRs)

One-dimensional 1,2-Sn(BDT)₂ NRs were synthesized by a facile solution reaction with the SnCl₄ as tin source and 1,2-benzenedithiol as complexing agent (Fig. 1a). Once 1,2-BDT encountered SnCl₄, the brownish red precipitate was immediately formed under an ice bath. The powder X-ray diffraction (PXRD) pattern in Fig. 1c shows the high crystallinity of 1,2-Sn(BDT)₂. The scanning electron microscope (SEM) reveals its one-dimensional structure observed in Fig. 1d with the length of 10 μm. This unique structure promotes the electron transfer during the electrocatalysis and exposes more active sites [26,32,33]. The results from energy-dispersive spectroscopy (EDS) in Table S1 reveal that the S/Sn ratio is around 3.86, which is close to the theoretical value (4). And the homogeneous distributions of Sn, S, and C elements are confirmed by mapping image (Fig. 1e & S2). The transmission electron microscope (TEM) image also confirms its uniform 1D morphology and the high-resolution imaging indicates that 1,2-Sn(BDT)₂ NRs are composed by finely dispersed nanoparticles with a homogeneous particle size of 2.48 ± 0.44 nm, as shown in Fig. 1f & g. The lattice fringes with a distance of 0.32 and 0.36 nm are clearly observed and consistent with the XRD data. Consequently, the hierarchical structure of 1,2-Sn(BDT)₂ NRs is illustrated in Fig. 1b.

In order to detect the content of non-metal element, the inductively coupled plasma atomic emission spectroscopy (ICP-AES) was measured (see in Table S2). The atomic ratio of C, H, and S approaches the theoretical value (3:2:1). Therefore, the chemical formula of the as-prepared 1,2-Sn(BDT)₂ is consistent with the expected value (C₁₂H₈S₄Sn). In order to resolve the detailed atomic-scale structure, the aberration-corrected high-angle annular dark field scanning TEM (HAADF-STEM) imaging was then performed (Fig. 1h). A number of bright spots represent the homogeneous 1,2-Sn(BDT)₂ nanoparticles less than six layers. The weight loss and differential thermal analysis (Fig. S3a) presents that 1,2-Sn(BDT)₂ starts to thermally decompose at 230 °C with two obvious weight losses, which are attributed to the decomposition of BDT ligand and volatilization of S species.

In addition, X-ray photoelectric spectroscopy (XPS) was conducted to study the chemical constituents. As shown in Fig. S4, the complex contains Sn, C, S, and O elements. In the high-resolution Sn 3d spectrum (Fig. 1i), two peaks are observed at 495.67 and 487.20 eV, corresponding to the Sn-S 3d_{3/2} and 3d_{5/2}, respectively. And the gap between two peaks is consistent with reported works for Sn⁴⁺ [34]. Moreover, the peaks at 495.04 and 486.65 eV are attributed to Sn-O 3d_{3/2} and 3d_{5/2} respectively, which is due to the oxidation of 1,2-Sn(BDT)₂ in air during the test. The high-resolution S 2p spectrum (Fig. 1j) is divided into subpeaks at 163.58 and 162.41 eV, corresponding to the S-Sn 2p_{1/2} and 2p_{3/2}, respectively. Because no other cations are detected in the XPS, we

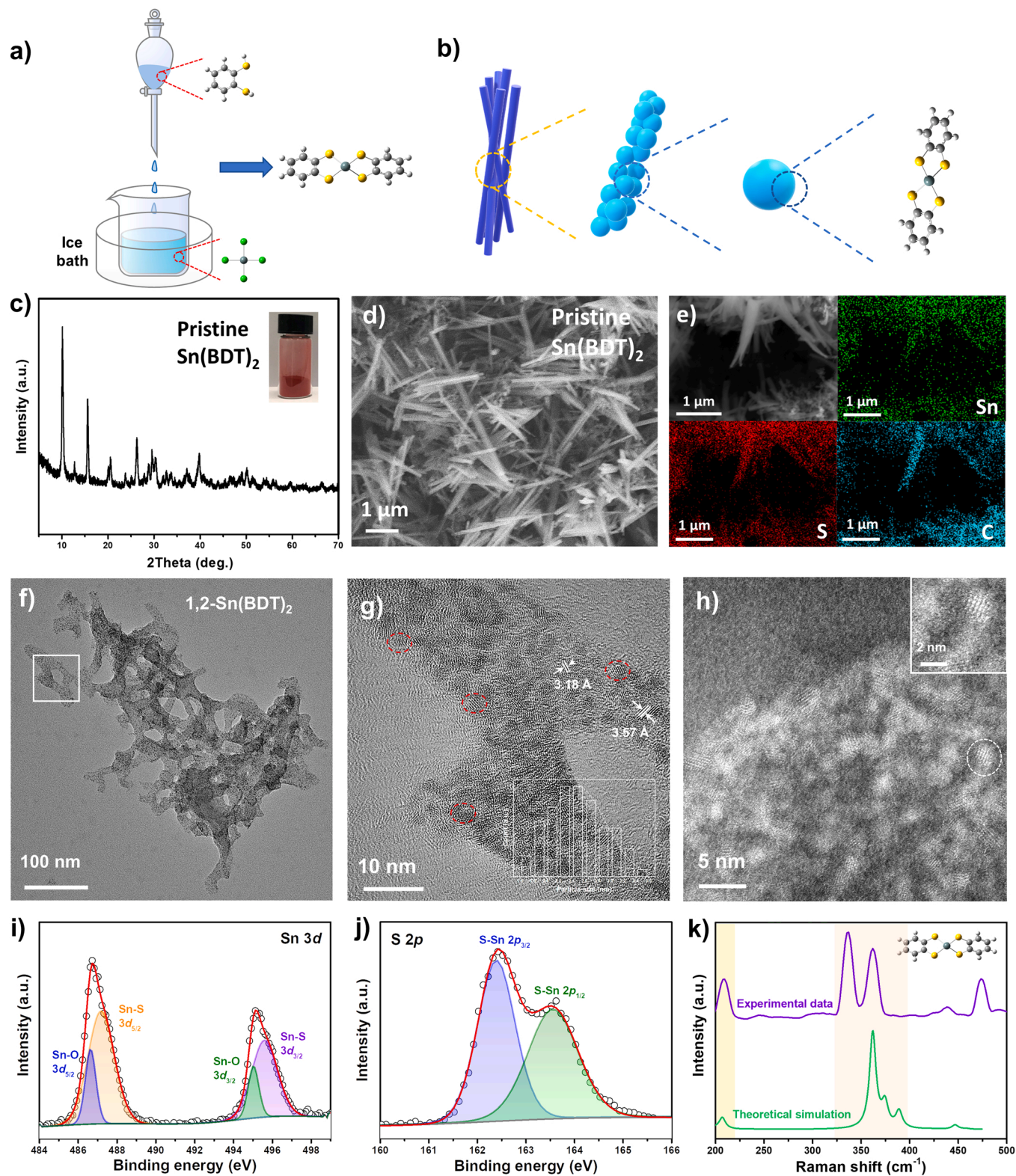


Fig. 1. Structural and compositional characterizations of 1,2-Sn(BDT)₂ NRs. (a) Schematic illustration on the synthesis of 1,2-Sn(BDT)₂, and gray, white, yellow, and green balls represent carbon, hydrogen, sulfur, and tin atom, respectively. (b) Schematic illustration on the structure of hierarchical 1,2-Sn(BDT)₂ NRs. (c) PXRD patterns of 1,2-Sn(BDT)₂. SEM image (d), and elemental mapping images (e) of 1,2-Sn(BDT)₂. Different magnification of TEM images (f–g), the inset is the particle size distribution. (h) HAADF-STEM image of 1,2-Sn(BDT)₂. XPS spectra for Sn 3d spectrum (i), and S 2p spectrum (j). (k) Experimental and simulated Raman spectra of 1,2-Sn(BDT)₂. Inset: model used for simulation.

suggest a neutral chelate in which 1,2-BDT is a -2 charged radical ligand, which is in agreement with other metal-dithiolene complexes [35,36]. Consequently, $1,2\text{-Sn}(\text{BDT})_2$ is a neutral coordination compound in which each Sn^{4+} is chelated by four S atoms.

In order to figure out the origin of the vibration modes, the IR and Raman spectra of $1,2\text{-Sn}(\text{BDT})_2$ were simulated by density functional theory (DFT), as deposited in Fig. 1k & S3c. The theoretical results show that Sn^{4+} coordinates well with two BDT molecules forming four identical Sn-S covalent bonds with the length of 2.39 \AA , and the electron localization function (ELF) analysis shows the Mayer bond order of Sn-S is 1.06 (Fig. S5b). It is clear to see the Sn-S vibration modes are mainly spread below 500 cm^{-1} , the IR activity of stretching and scissor vibrations for Sn-S are 480.4 and 222.6 cm^{-1} , respectively, and the Raman activity corresponding to 382.0 and 144.1 cm^{-1} , respectively. It is worth to note that the S-H vibration peak at 2537 cm^{-1} vanishes in $1,2\text{-Sn}(\text{BDT})_2$, indicating that the thiol group of 1,2-BDT first reacted with the hydroxyl group in $\text{Sn}(\text{OH})_4$ from the hydration of SnCl_4 , then the

exposed Sn^{4+} was coordinated with 1,2-BDT to form the Sn-BDT complex.

3.2. In situ electrochemical conversion of $1,2\text{-Sn}(\text{BDT})_2$ to sulfur doped Sn nanoclusters (Sn NCs:S)

We attempted to electrochemically reduce $1,2\text{-Sn}(\text{BDT})_2$ and interrogated the composition and microstructure of reduced counterpart. CV tests were performed in CO_2 -saturated 0.5 M KHCO_3 at 50 mV s^{-1} . As depicted in Fig. 2a, a series of reduction peaks from -0.7 to $-1.3 \text{ V}_{\text{Ag/AgCl}}$ are presented. There are two distinguishable peaks located at -0.85 and $-1.15 \text{ V}_{\text{Ag/AgCl}}$, which are attributed to the reduction of Sn^{4+} to Sn^{2+} and metallic Sn species, respectively [10,37]. After the reduction process, the reddish-brown sample turns to black materials, seen in Fig. S7a. It is worth noting that currents in the region from -1.4 to $-1.8 \text{ V}_{\text{Ag/AgCl}}$ decrease notably and become stable after 10 cycles (Fig. S6). This overall reaction is supposed to be written as the following:

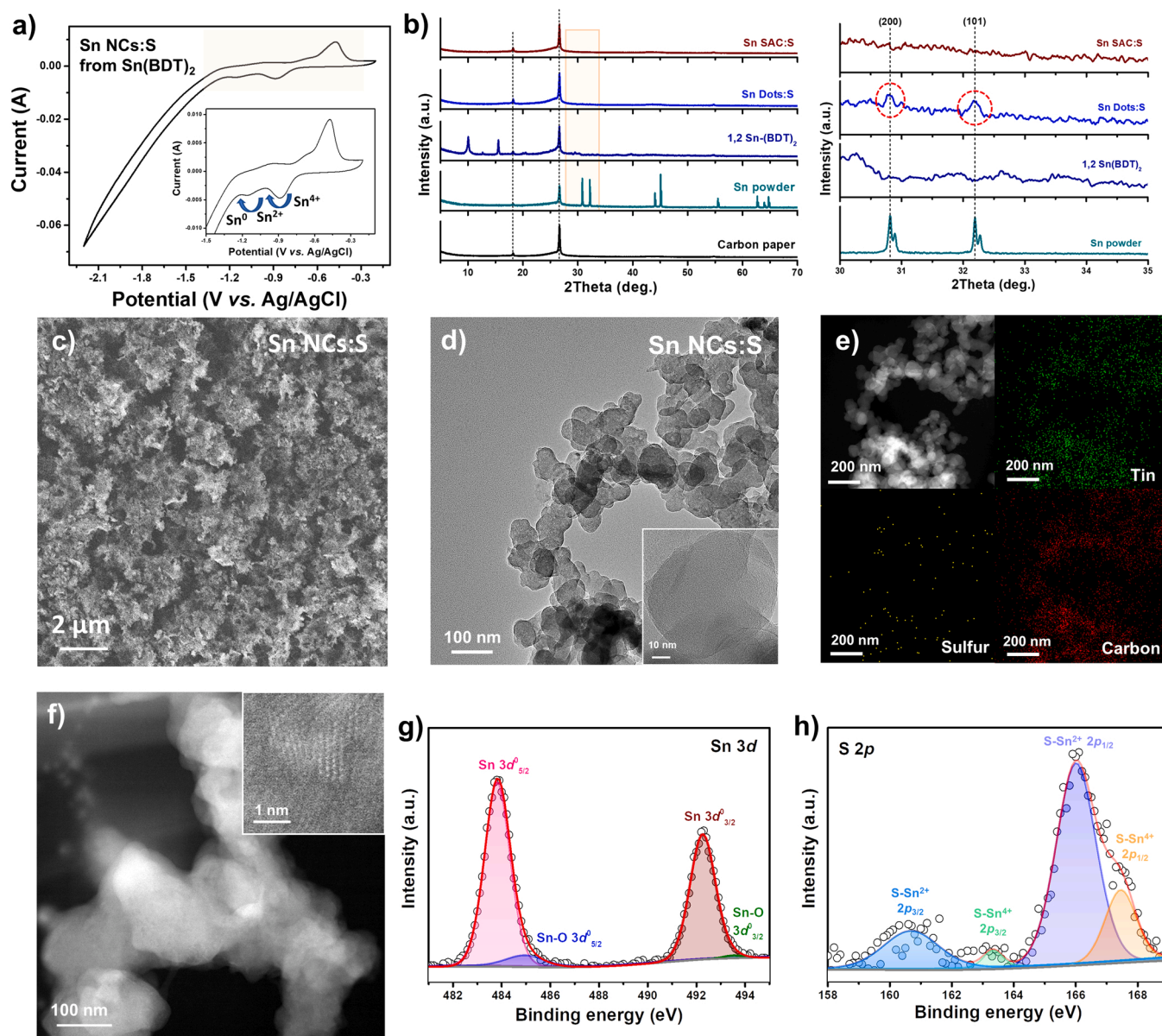
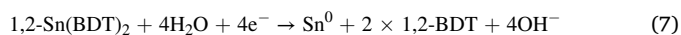


Fig. 2. In situ electrochemical conversion of $1,2\text{-Sn}(\text{BDT})_2$ to Sn NCs:S. (a) CV curves of $1,2\text{-Sn}(\text{BDT})_2$ in CO_2 -saturated 0.5 M KHCO_3 . (b) XRD patterns of $1,2\text{-Sn}(\text{BDT})_2$, Sn NCs:S with the different reduction times (Sn Dots:S for 20 min, and Sn SAC:S for 2 h), and the contrast samples of carbon paper and Sn powder. The diffraction peaks at the dotted line come from the signal of carbon paper substrate. SEM image (c), TEM images (d), HAADF image and elemental mapping of Sn NCs:S (e). HAADF-STEM image (f) reveals the atomic microstructure. Sn 3d spectrum (g), and S 2p spectrum (h) of Sn NCs:S.



To characterize the structure of reduced electrocatalyst, several measurements were conducted. As shown in Fig. 2b, the diffraction peaks of Sn NCs:S samples with the reduction time of 20 min and 2 h are distinctly different from 1,2-Sn(BDT)₂. Compared with the XRD data of metallic Sn, Sn NCs:S reduced with 20 min unveils the pronounced peaks at 30.8 and 32.2°, which are assignable to the (200) and (101) planes of tetragonal Sn (PDF#04-0673). With the extension of reduction time, the XRD data of Sn NCs:S vanish at the crystalline Sn region, suggesting the possibility of smaller size or amorphous structure. To explore the whereabouts of S-containing ligand, the catholytes before and after the electroreduction were performed by ¹H NMR, as presented in Fig. S7c. The result reveals that S-containing ligand is released into the solution and confirms the redox reaction.

From the SEM image of Sn NCs:S (Fig. 2c), there is no noteworthy Sn nanoparticle. In addition, the evolution process of in situ reduced Sn-based materials was investigated by SEM images (Fig. S8 & S9). The nanorods of 1,2-Sn(BDT)₂ change to nanoparticles and amorphous materials eventually with the extension of reduction time. According to Fig. S10, tin, carbon, and traces of sulfur are distributed uniformly in reduced catalysts. Furthermore, the microstructure of Sn NCs:S represented by TEM images (Fig. 2d), exhibits the homogeneous spherical nanoparticles without obvious Sn agglomerations. The equipped EDS with HAADF-STEM also shows the uniform distribution of Sn, C, and residual S elements (Fig. 2e & S11). According to the SEM-EDX and TEM-EDS data in Table S4, Sn NCs:S can be denoted as SnS_{0.08} and SnS_{0.10}, respectively. The trace of sulfur originates from the adsorbed S-containing ligand. From the aberration-corrected HAADF-STEM image (Fig. 2f), Sn NCs:S is composed of three to four atomic layers, indicating its successful synthesis.

To investigate the valence state, XPS data are given in Fig. 2g-h. After the electroreduction, the surface signal of sulfur in Sn NCs:S is suppressed markedly compared with 1,2-Sn(BDT)₂ in the survey spectrum (Fig. S12a), indicating the occurrence of reduction reaction. Metallic Sn dominates the surface of Sn NCs:S demonstrated by the main

peaks located at 483.8 and 492.2 eV, which are assigned to Sn⁰ 3d_{5/2} and 3d_{3/2}, respectively. In S 2p spectrum, the tiny peaks of 160.7 and 166.0 eV are assigned to the S²⁻ species that are attached to Sn²⁺, while two peaks located at 163.4 and 167.5 eV correspond to the 2p_{3/2} and 2p_{1/2} of [SnS₂] configuration, respectively. To investigate the electrochemical performance of Sn NCs:S, the contrast samples with different content of sulfur (Sn powder and SnS₂ nanosheets) are also conducted, and their physicochemical properties are shown in Fig. S13 & S14.

3.3. Experimental evaluation of CO₂ electroreduction

To evaluate the performance of Sn NCs:S, the catalyst are tested in a gas-tight H-cell. In order to investigate the influence of reduction time to CO₂RR performances, LSV curves of reduced Sn-based species were performed (Fig. S15). With the extension of reduction time, the current densities increase obviously with enhanced electrical conductivity in less than two hours. Particularly, the polarization curves of Sn NCs:S exhibit a cathodic current onset at -0.46 V_{RHE}, and then continuously increase to 32 mA cm⁻² at -1.00 V_{RHE} (Fig. 3a), which are larger than other Sn-based materials [8,15,29]. In the N₂-saturated solution, the apparent currents are dominated by the hydrogen evolution reaction (HER) and the performances of Sn-based electrocatalysts are diminished with more negative onset potentials and smaller current densities, attesting to their poor HER activities. Considering the difference between N₂- and CO₂-saturated electrolytes, Sn NCs:S exhibits remarkably enhanced CO₂RR performance over Sn NPs and SnS₂. Furthermore, electrolysis was performed at several selected potentials for over 4 h to analyze reduction products for different electrocatalysts (Fig. S16–19). The gaseous products were measured by a gas chromatograph (GC), and liquid products were measured by internal standard method of ¹H NMR (Fig. S20).

Quantified by the above analysis, the products include formate, CO, and H₂ over Sn NCs:S (Fig. 3b). At -0.98 V_{RHE}, Sn NCs:S exhibited the highest FE of 80% for formate production. Meanwhile, it produces CO with the highest FE of 17% and suppresses HER process. Overall, the FE for C₁ product reaches 90% at -0.97 V_{RHE} (Fig. S21), better than other

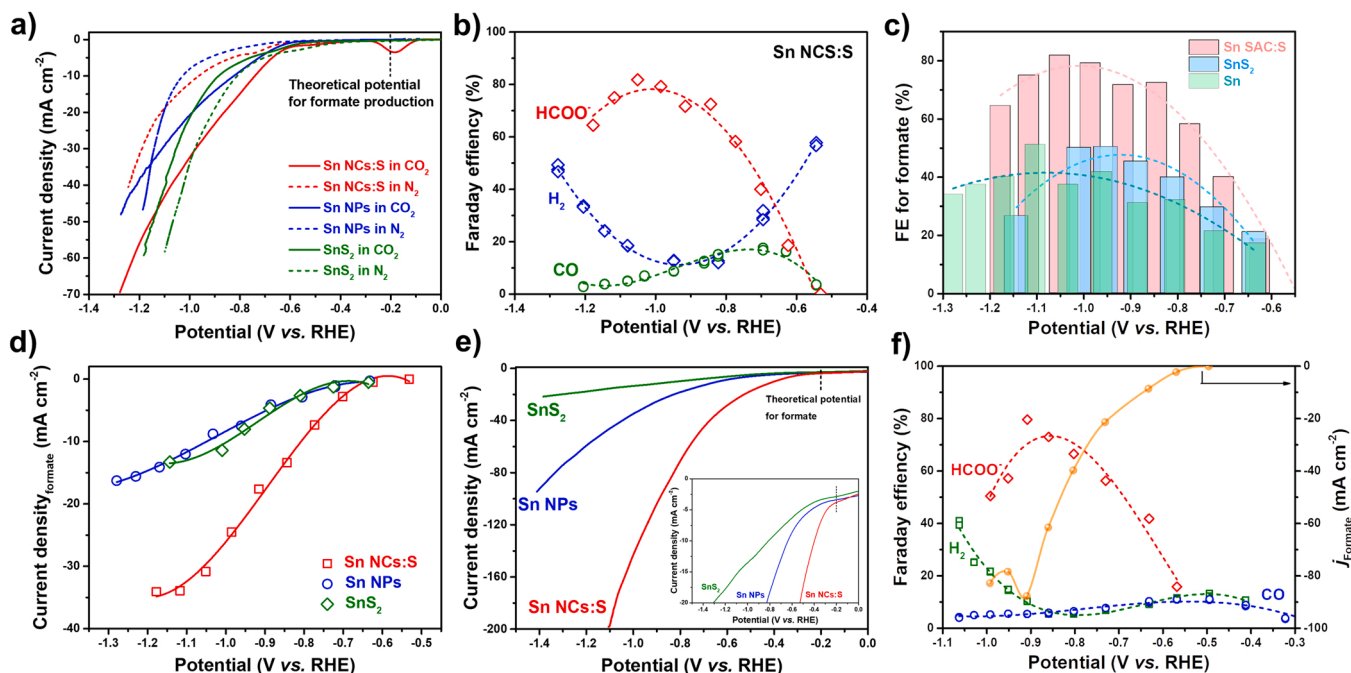


Fig. 3. Electrochemical performance of Sn NCs:S, Sn NPs, and SnS₂ NSs towards CO₂RR to C₁ products. (a) Polarization curves of Sn NCs:S and the contrast samples in N₂- and CO₂-saturated 0.5 M KHCO₃; (b) Faradaic efficiencies of HCOO⁻, H₂, CO over the Sn NCs:S; (c) Faradaic efficiencies for formate production for Sn NCs:S, Sn NPs, and SnS₂ NSs; (d) Comparison on the formate partial current density over Sn-based electrocatalysts; (e) Polarization curves of Sn-based electrocatalysts for CO₂RR using the flow cell; (f) FEs of carbonaceous products over Sn NCs:S with the formate partial current density.

reported Sn-based electrocatalysts [8,23]. The FEs of formate for three Sn-based electrocatalysts with different sulfur contents are further compared (Fig. 3c). The enhanced activities for Sn NCs:S over 30–40% than other Sn-homologous materials indicate that the small amount of sulfur has positive effect to the performance. As shown in Fig. 3d, Sn NCs:S generates the formate partial current density of 34.2 mA cm^{-2} at $-1.17 \text{ V}_{\text{RHE}}$, which is double of the values for Sn NPs and SnS_2 . Interestingly, this value of Sn NCs:S is also superior to most of Sn-based catalysts [10,15,27,28,38] (Fig. S22). The enhanced catalytic performance of Sn NCs:S is also confirmed by the current density or formate partial current density per unit of Sn mass than those of Sn and SnS_2 (Fig. S23). Therefore, these results demonstrate that Sn NCs:S represents one of the best catalysts for formate production.

Tafel analysis is an effective approach to reveal the kinetics of catalytic process (Fig. S23c). The Tafel slopes of Sn NCs:S (126 mV dec^{-1}) and Sn NPs (202 mV dec^{-1}), is smaller than SnS_2 (270 mV dec^{-1}), which is consistent with reported formate-producing catalysts [11,39]. Moreover, Tafel slope of Sn NCs:S is close to 118 mV dec^{-1} , indicating that the activation of CO_2 serves as the rate-limiting step [6]. Thus, Sn with the trace of sulfur exhibits faster kinetic than those of Sn and SnS_2 . In order to verify the binding affinity of the CO_2^{*} intermediate, adsorption of OH^- as a surrogate ion was examined (Fig. S24) [10]. A stronger adsorption affinity of OH^- ion on the metallic Sn is demonstrated by lower potential than SnS_2 . Furthermore, the trace amount of sulfur improves the binding affinity for monovalent anion, which is concluded by the difference between Sn NCs:S and Sn. Therefore, the organosulfide-derived Sn might introduce efficient stabilization for CO_2^{*} intermediate, thus facilitating formate production.

The EIS results with the equivalent circuit model are used to analyze the conductivity characteristics (Fig. S23d and Table S5). The semicircle located at low frequency region represents the charge transfer resistances (R_{CT}) [40]. The contribution of intrinsic resistance (R_s) and R_{CT} of SnS_2 (7.69Ω) is reduced to 5.92Ω (Sn NPs) and further significantly to 2.70Ω for Sn NCs:S, indicating a facilitated electrochemical performance owing to the metallic feature. ECSAs are identified by double-layer capacitances (C_{dl}) determined through CV measurements (Fig. S25). Sn NCs:S provides larger ECSA (9.39 cm^2) than those of Sn NPs (5.40 cm^2) and SnS_2 (5.36 cm^2). Taking ECSA as the normalization, Sn NCs:S also exhibits an enhanced activity than other two catalysts (Fig. S26), thus definitely verifying the promotion of trace sulfur to CO_2RR . The distensible ECSA of Sn NCs:S is also validated by the calculated Connolly surface areas of S-doped tin [30]. It was found that slight doping (12.5%) of sulfur increased the atomic surface area compared with pure tin by 13%. Consequently, the slight doping of sulfur could induce high accessibility and more undercoordinated sites.

Durability is a significant factor towards practical application. Stability was measured by chronopotentiometry for 10 h at 30 mA cm^{-2} , Sn NCs:S exhibits less than 10% change of the potential (Fig. S27a), better than Sn NPs (17% attenuation). In terms of the selectivity, activity, and stability towards formate production, the comprehensive performance of Sn NCs:S places on the top of Sn-based electrocatalysts, such as metal-based [15,38,41–43], alloy-based [8,44,45], oxide-based [10,11,46], and chalcogenide-based [27,29], as shown in Table S7. Conventional CO_2RR catalysts for formate production include Bi-based [18,47–49], In-based [50], Sb-based [51], and carbon materials [37, 52,53]. Noteworthy is that Sn NCs:S also outperforms above CO_2RR electrocatalysts, especially the formate partial current density (Table S8).

In order to explore the physicochemical change for Sn NCs:S during CO_2RR , several postmortem characterizations were performed. As shown in Fig. S28, there is no obvious growth of Sn nanoparticles, indicating that the high dispersion of tin nanoclusters remained during electrocatalysis. Moreover, the elemental distributions of tin and sulfur are still uniform based on the EDS data. After long-term electrocatalysis, Sn NCs:S exhibits the Raman peaks located at 120 and 190 cm^{-1} , which are attributed to the metallic Sn [54]. The Sn 3d spectrum after the

durability demonstrates that the chemical states of Sn^0 in Sn NCs:S exhibit negligible change (Fig. S29). In addition, the sulfur signal after the electrocatalysis weakens, suggesting the slight loss of sulfur doping.

To satisfy the requirement for CO_2 utilization, the current density should reach 200 mA cm^{-2} . And conventional H-type cell barely achieves this target owing to the limited CO_2 concentration [55]. Consequently, Sn NCs:S loaded on GDE was evaluated using the flow cell to accelerate the diffusion and solubility of CO_2 [56]. When tested in 1 M KOH, the onset overpotential of Sn NCs:S is reduced to be lower than 50 mV, smaller than those of Sn NPs and SnS_2 . It is most incredible that its current density reaches ca. 200 mA cm^{-2} at $-1.10 \text{ V}_{\text{RHE}}$, meeting the commercialization requirement (Fig. 3e). The formate activity and selectivity are also satisfactory, and measured to be 80% at $-0.90 \text{ V}_{\text{RHE}}$ with the minimal $\text{FE}_{\text{hydrogen}}$ of 5.30% (Fig. 3f). Therefore, its formate partial current density reaches the maximum of $-88.26 \text{ mA cm}^{-2}$ at the overpotential of 710 mV. Finally, the durability of Sn NCs:S shows to sustain at $-0.71 \text{ V}_{\text{RHE}}$ in 1 M KOH for over 50 h (Fig. S27b). Compared with other Sn-based analogs, Sn NCs:S manifests robust stability and opens the possibility for the practical application. After the 50-h electrolysis, formate was accumulated in the cathode counterpart, confirmed by the pH change of catholyte. According to the NMR data (Fig. S30), the productive rate for formate is $136.69 \mu\text{mol cm}^{-2} \text{ h}^{-1}$ at $-0.71 \text{ V}_{\text{RHE}}$.

3.4. The promoting effect of trace sulfur towards CO_2RR

In order to investigate the structural evolution during the electroreduction of 1,2-Sn(BDT) $_2$ and CO_2RR , in situ XRD was performed to circumvent the distraction of external environment. As depicted in Fig. S32a, the peak of 1,2-Sn(BDT) $_2$ located at 54.1° fades away lower than $-1.0 \text{ V}_{\text{Ag/AgCl}}$, which is attributed to the formation of metallic Sn. Moreover, several peaks at 38.9 , 41.2 , and 47.8° are increasingly obvious with the negative scan and remain during CO_2RR process, illustrating the electrochemical stability of Sn NCs:S. In situ Raman spectra usually reflect the reaction intermediate during electrocatalysis (Fig. S32b). The signals located at 205.8 , 360.9 , 472.1 , 1099.5 , 1435.3 , and 1546.5 cm^{-1} are attributed to the pristine 1,2-Sn(BDT) $_2$, then disappear gradually at $-1.2 \text{ V}_{\text{Ag/AgCl}}$. Finally, the peaks of 1361.4 , and 1597.7 cm^{-1} at the potential lower than $-2.0 \text{ V}_{\text{Ag/AgCl}}$, which are probably assigned to the D and G band of carbon substrate. During the CO_2RR process, there are no obvious peaks of metallic Sn, illustrating that Sn NCs:S maintains its nanocluster feature and electrochemical stability.

Although metallic Sn is the active species for CO_2RR in Sn NCs:S, the promoting effect of the trace sulfur doping should be studied in depth. To investigate this structure-activity relationship, a trace amount of Zn^{2+} was introduced in SnS_2 to block the surface S sites. When SnS_2 soaked in the $0.14 \text{ mM Zn(NO}_3)_2$ solution with different times, the sulfur content decreased prominently in one minute based on the SEM-EDX data (Fig. S33). As shown in Figs. S34c and 4a, the HER activity (current density in N_2 -saturated electrolyte) decreased obviously in less than 5 s, suggesting the positive effect of surface $\text{S}_{\text{ad}}^{\delta-}$ on promoting HER activity on Sn-based materials, which was also reported in Ni-based electrocatalysts [57]. While in the CO_2 -saturated electrolyte, the electrocatalytic reaction includes CO_2RR and HER simultaneously. The abnormal current densities for the samples with less than 5 s in the potential range of -0.6 to $-1.0 \text{ V}_{\text{RHE}}$ indicate the promotion effect of trace sulfur to CO_2RR . According the evolution of equivalent series resistance (ESR), the electroconductibility of SnS_2 with less sulfur content increases obviously in CO_2 environment while it slightly increases in N_2 , suggesting that sulfur on the surface can facilitate electron transfer and accelerate the catalytic process. Lim et al. confirmed that sulfur or arsenic doping effectively minimize the overpotential with good electrochemical stability [58]. The major effect of p-block dopants imposes partial covalency into the metal catalysts, thereby enhancing their catalytic activity.

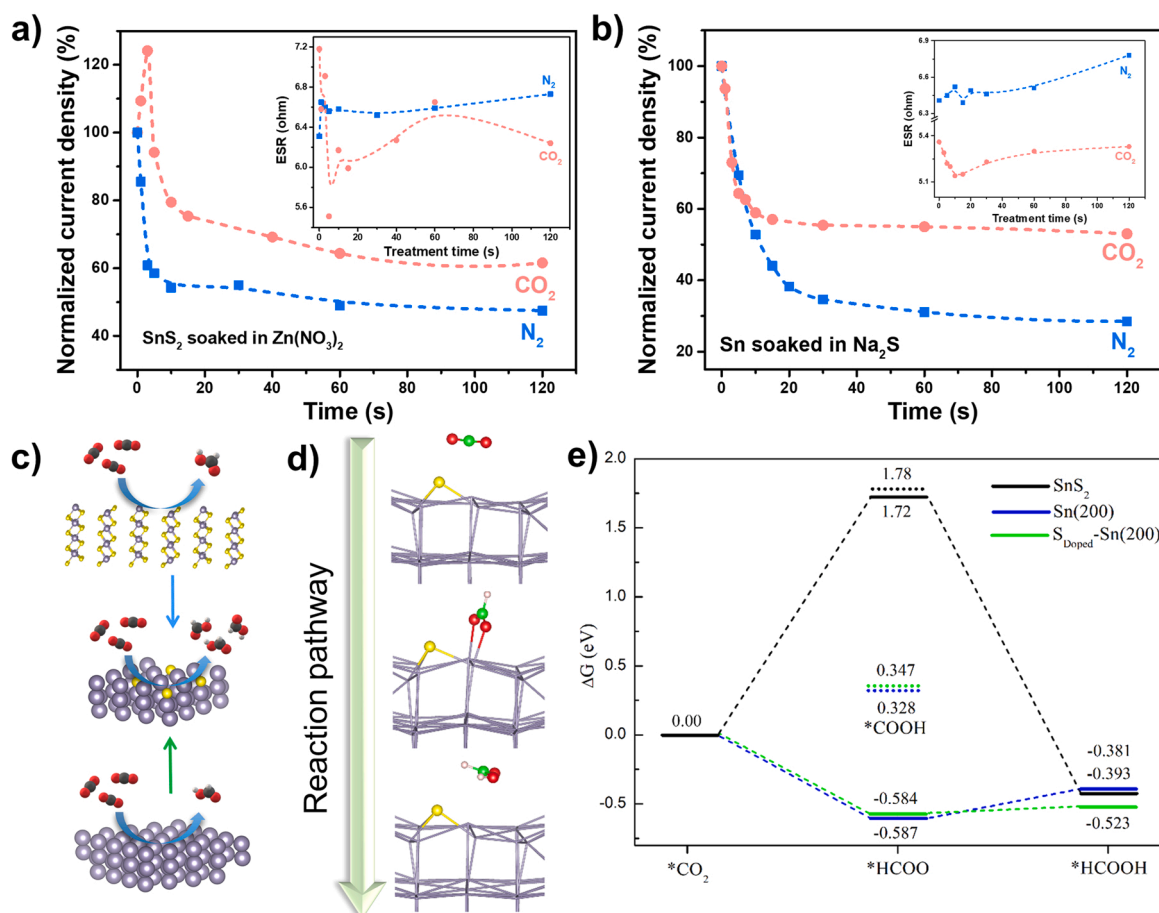


Fig. 4. The effect of sulfur to the CO_2RR performance and corresponding theoretical validation. (a) The function of normalized current densities at $-0.90 \text{ V}_{\text{RHE}}$ with the different soaking time of SnS_2 in $\text{Zn}(\text{NO}_3)_2$, the inset is the relationship of the EIS data with the treatment time; (b) The function of normalized current densities at $-1.15 \text{ V}_{\text{RHE}}$ with the different soaking time of Sn in Na_2S , the inset is the relationship of the EIS data with the treatment time; (c) Schematic diagram for the effect of sulfur to the electrocatalytic performance; (d) The detailed structure of intermediate state during CO_2 reduction to HCOOH ; (e) Gibbs free energy difference diagrams of CO_2RR to HCOOH . The Gibbs free energy of CO_2 adsorbed at substrate slab is set at zero eV. It should be noted that the intermediate appears some difference, as the solid line represents HCOO^* and dotted line represents COOH^* . The gray, pink, red, and green balls represent Sn, H, O, and C atom, respectively.

These above results unambiguously demonstrated the promotion effect of the trace surfur toward CO_2RR . Surface modification of Sn NPs with a trace amount of $\text{S}_{\text{ad}}^{\delta-}$ was further performed to prove the above analysis. The content of sulfur increased distinctly with the extension of Sn NPs soaked in 0.5 mM Na_2S solution. As shown in Fig. 4b, CO_2RR activity of metallic Sn was improved with the addition of surface sulfur, which is proved by the smaller current falloff in CO_2 than that of N_2 . Moreover, Sn NCs:S with the sulfur content of 8%, deactivation was then observed when the soaking time in $\text{Zn}(\text{NO}_3)_2$ solution less than 15 s, suggesting that approximate zero $\text{S}_{\text{ad}}^{\delta-}$ inhibited the CO_2RR activity of Sn^0 (Fig. S35). And ESR value decreases slightly along with the soaking time synchronously. These results demonstrate that low surface coverage of $\text{S}_{\text{ad}}^{\delta-}$ promotes the CO_2RR activity, and excess $\text{S}_{\text{ad}}^{\delta-}$ blocks the active sites and encumbers the performance, as illustrated in Fig. 4c. And this promoting effect for sulfur dopant are confirmed by Sargent [59], which it is revealed that the sulfur- CO_2 intermediate state in TiS_2 thin films steers the reduction kinetics toward mainly CO.

3.5. The proposed mechanism of sulfur doping to CO_2RR

To further understand the activity of trace S towards formate formation, the first-principles calculations were carried out via the CHE approach. In order to model the detailed reaction process, possible Sn crystal faces are examined according to surface energy. Clearly, Sn (200) surface has a lower energy surface at about $0.03 \text{ eV}/\text{\AA}^2$ (Fig. S36).

According to the experiment and calculation result, the Sn (200) plane is used to model the substrate (Fig. S37a), while the (2×3) supercell with four layers is orthogonal lattice. Based on this supercell, the minor S-doping configuration can be obtained by introducing one S interstitial atom at Sn (200) surface to model the S-doped Sn. The detailed doping sites including surface and subsurface have been checked (Fig. S38). The initial calculations show that S atom prefers to locate on the surface forming three-coordination as seen in sur-1 site. For SnS_2 sheet, a (3×3) supercell is adopted with the hexagonal crystal for further calculation, since it can provide enough surface-active site.

Theoretically, CO_2 conversion to HCOOH involves two proton/electron transfer steps. Firstly, CO_2 is adsorbed on the substrate, followed by one proton and one electron attacking to form HCOO^* intermediate. Then the HCOOH was finally produced by the additional proton/electron transformation, and the intermediate along the reaction path are depicted in Fig. 4d. Thus CO_2 adsorption behavior is preferentially investigated. The results show that CO_2 adsorption energies on these substrates are -0.445 eV (Sn surface), -0.202 eV ($\text{S}_{\text{Doped}}\text{-Sn}$ surface), and -0.110 eV (SnS_2). Followed by the adsorption, for HCOO^* (Table S9), there are obvious difference on the different substrates. The adsorption energy is -3.060 and -2.820 eV for Sn- and $\text{S}_{\text{Doped}}\text{-Sn}$ and -0.378 eV for SnS_2 . It is clear to see the adsorption energy of HCOO^* at $\text{S}_{\text{Doped}}\text{-Sn}$ is neither too weak nor too strong, thus the catalytic performance of $\text{S}_{\text{Doped}}\text{-Sn}$ is better than those of two substrates.

In addition to the adsorption behavior, the Gibbs free energies for

intermediate states are further investigated. From Fig. 4e, it is found that the protonation of C atom to the $^*\text{COOH}$ intermediate are mildly endothermic for the three cases with 0.328 eV (Sn), 0.347 eV ($\text{S}_{\text{Doped-Sn}}$), and 1.78 eV (SnS_2). Whereas the formation of $^*\text{HCOO}$ intermediate becomes completely different, exothermic for Sn (-0.587 eV) and $\text{S}_{\text{Doped-Sn}}$ (-0.584 eV) but strongly endothermic at SnS_2 surface (1.72 eV), which indicates CO_2 may be easier to form $^*\text{HCOO}$ intermediate on Sn-based materials. Consecutively, forming HCOOH are endothermic at SnS_2 , while it is exothermic at the Sn surface. Then, a rate determining step occurs at the conversion of $^*\text{HCOO}$ to $^*\text{HCOOH}$ with an energy barrier at -0.061 eV for $\text{S}_{\text{Doped-Sn}}$, and 0.206 eV for Sn surface. Unlike these cases, the rate determining step for SnS_2 locates at $^*\text{CO}_2 \rightarrow ^*\text{HCOO}$ step with an energy barrier of 1.72 eV, which is extremely larger than above two species. Based on the discussions, it clearly shows that $\text{S}_{\text{Doped-Sn}}$ surface has the lowest energy barrier and highest activity, which is consistent with the experimental result. Therefore, both adsorption behavior and Gibbs free energy difference effectively exhibit higher activity of $\text{S}_{\text{Doped-Sn}}$ surface for CO_2 conversion to HCOOH .

4. Conclusion

In summary, we report the preparation of Sn nanoclusters with trace of sulfur doping (Sn NCs:S) from 1,2-Sn(BDT) $_2$. As a CO_2 RR electrocatalyst, it enables the efficient CO_2 reduction to C_1 feedstock with the satisfactory selectivity (90%), and large partial current density towards formate (35 mA cm^{-2} at $-1.1 \text{ V}_{\text{RHE}}$). Compared with metallic Sn and SnS_2 , it exhibits an astonishing formate partial current density. More interestingly, it achieves a comparably high current density (200 mA cm^{-2} at $-1.1 \text{ V}_{\text{RHE}}$), and prolonged durability (over 50 h). The enhanced activity during the CO_2 conversion is attributed to the increased active sites caused by the atomic dispersion and the promoting influence induced by the trace of sulfur doping. Insights into the electrochemical presentations of the surface sulfur to the CO_2 RR performance are assessed with the different sulfur (de)doping of Sn and SnS_2 catalysts. According to DFT calculations, as the incorporation of S doping to the Sn catalysts, the $^*\text{HCOOH}$ intermediate is stabilized compared to the counterpart without S doping, which facilitates the electrochemical activity and selectivity. This study opens up an attractive avenue to design highly dispersed electrocatalysts for efficiently and stably converting CO_2 to C_1 chemicals.

CRedit authorship contribution statement

Xin Wang and Fengli Li: Investigation, Methodology, Formal analysis, Validation, Writing – original draft. **Wen-Jin Yin and Yubing Si:** Formal analysis, Visualization, Validation, Writing – original draft. **Ming Miao:** Methodology, Formal analysis, Validation, Writing – original draft. **Xiaoming Wang:** Formal analysis, Writing – review & editing. **Yongzhu Fu:** Supervision, Conceptualization, Data curation, Writing – review & editing.

Declaration of Competing Interest

The authors declare that they have no known competing financial interests or personal relationships that could have appeared to influence the work reported in this paper.

Acknowledgement

This work was financially supported by the China Postdoctoral Science Foundation (2019M650173), the National Natural Science Foundation of China (Grant Nos. 21975225 and 51902293), and Zhengzhou University.

Appendix A. Supporting information

Supplementary data associated with this article can be found in the online version at doi:10.1016/j.apcatb.2021.120936.

References

- [1] T. Letcher, Climate Change: Observed Impacts on Planet Earth, Elsevier, Amsterdam, 2009.
- [2] Christina W. Li, Jim Ciston, Matthew W. Kanan, Electroreduction of carbon monoxide to liquid fuel on oxide-derived nanocrystalline copper, *Nature* 508 (2014) 504–507.
- [3] M. Asadi, B. Kumar, A. Behranginia, B.A. Rosen, A. Baskin, N. Repnin, D. Pisasale, P. Phillips, W. Zhu, R. Haasch, R.F. Klie, P. Král, J. Abiade, A.S. Khojin, Robust carbon dioxide reduction on molybdenum disulphide edges, *Nat. Commun.* 5 (2014) 4470.
- [4] K. Manthiram, B.J. Beberwyck, A.P. Alivisatos, Enhanced electrochemical methanation of carbon dioxide with a dispersible nanoscale copper catalyst, *J. Am. Chem. Soc.* 136 (38) (2014) 13319–13325.
- [5] M. Chen, J.C. Wu, C.C. Lu, X. Luo, Y.Q. Huang, B. Jin, H.X. Gao, X.W. Zhang, M. Argyle, Z.W. Liang, Photoreduction of CO_2 in the presence of CH_4 over g-C $_3$ N $_4$ modified with TiO $_2$ nanoparticles at room temperature, *Green Energy Environ.* 6 (2021) 938–951.
- [6] M. Dunwell, Q. Lu, J.M. Heyes, J. Rosen, J.G. Chen, Y.S. Yan, F. Jiao, B.J. Xu, The central role of bicarbonate in the electrochemical reduction of carbon dioxide on gold, *J. Am. Chem. Soc.* 139 (2017) 3774–3783.
- [7] M. Aresta, A. Dibenedetto, A. Angelini, Catalysis for the valorization of exhaust carbon: from CO_2 to chemicals, materials, and fuels. Technological use of CO_2 , *Chem. Rev.* 114 (2014) 1709–1742.
- [8] P.T. Wang, M. Qiao, Q. Shao, Y.C. Pi, X. Zhu, Y.F. Li, X.Q. Huang, Phase and structure engineering of copper tin heterostructures for efficient electrochemical carbon dioxide reduction, *Nat. Commun.* 9 (2018) 4933.
- [9] M.F. Baruch, J.E. Pander III, J.L. White, A.B. Bocarsly, Mechanistic insights into the reduction of CO_2 on tin electrodes using in situ ATR-IR spectroscopy, *ACS Catal.* 5 (2015) 3148–3156.
- [10] S. Zhang, P. Kang, T.J. Meyer, Nanostructured tin catalysts for selective electrochemical reduction of carbon dioxide to formate, *J. Am. Chem. Soc.* 136 (2014) 1734–1737.
- [11] Y.H. Chen, M.W. Kanan, Tin oxide dependence of the CO_2 reduction efficiency on tin electrodes and enhanced activity for tin/tin oxide thin-film catalysts, *J. Am. Chem. Soc.* 134 (2012) 1986–1989.
- [12] Y.H. Chen, C.W. Li, M.W. Kanan, Aqueous CO_2 reduction at very low overpotential on oxide-derived Au nanoparticles, *J. Am. Chem. Soc.* 134 (2012) 19969–19972.
- [13] C.W. Li, M.W. Kanan, CO_2 reduction at low overpotential on Cu electrodes resulting from the reduction of thick Cu_2O films, *J. Am. Chem. Soc.* 134 (2012) 7231–7234.
- [14] J.Y. Li, J.X. Li, X.L. Liu, J.C. Chen, P.F. Tian, S. Dai, M.H. Zhu, Y.-F. Han, Probing the role of surface hydroxyls for Bi, Sn and In catalysts during CO_2 reduction, *Appl. Catal. B Environ.* 298 (2021), 120581.
- [15] F.C. Lei, W. Liu, Y.F. Sun, J.Q. Xu, K.T. Liu, L. Liang, T. Yao, B.C. Pan, S.Q. Wei, Y. Xie, Metallic tin quantum sheets confined in graphene toward high efficiency carbon dioxide electroreduction, *Nat. Commun.* 7 (2016) 12697.
- [16] C.H. Lee, M.W. Kanan, Controlling H^+ vs. CO_2 reduction selectivity on Pb electrodes, *ACS Catal.* 5 (2015) 465–469.
- [17] N. Han, Y. Wang, H. Yang, J. Deng, J.H. Wu, Y.F. Li, Y.G. Li, Ultrathin bismuth nanosheets from in situ topotactic transformation for selective electrocatalytic CO_2 reduction to formate, *Nat. Commun.* 9 (2018) 1320.
- [18] X. Wang, W.-J. Yin, Y.B. Si, X.M. Wang, X.X. Guo, W. Guo, Y.Z. Fu, Conversion of CO_2 to chemical feedstocks over bismuth nanosheets in situ grown on nitrogen-doped carbon, *J. Mater. Chem. A* 8 (2020) 19938–19945.
- [19] Y.F. Sun, S. Gao, Y. Xie, Atomically-thick two-dimensional crystals: Electronic structure regulation and energy device construction, *Chem. Soc. Rev.* 43 (2014) 530–546.
- [20] J.Y. Chen, Z.J. Li, X.Y. Wang, X.H. Sang, S.X. Zheng, S.J. Liu, B. Yang, Q.H. Zhang, L.C. Lei, L.M. Dai, Y. Hou, Promoting CO_2 electroreduction kinetics on atomically dispersed monovalent Zn(I) sites by rationally engineering proton-feeding centers, *Angew. Chem. Int. Ed.* (https://doi.org/10.1002/anie.202111683).
- [21] X.Y. Wang, X.H. Sang, C.-L. Dong, S.Y. Yao, L. Shuai, J.G. Lu, B. Yang, Z.J. Li, L. C. Lei, M. Qiu, L.M. Dai, Y. Hou, Proton capture strategy for enhancing electrochemical CO_2 reduction on atomically dispersed metal–nitrogen active sites, *Angew. Chem. Int. Ed.* 60 (2021) 11959–11965.
- [22] X.Y. Wang, Y. Wang, X.H. Sang, W.Z. Zheng, S.H. Zhang, L. Shuai, B. Yang, Z.J. Li, J.M. Chen, L.C. Lei, N.M. Adli, M.K.H. Leung, M. Qiu, G. Wu, Y. Hou, Dynamic activation of adsorbed intermediates via axial traction for the promoted electrochemical CO_2 reduction, *Angew. Chem. Int. Ed.* 60 (2021) 4192–4198.
- [23] D.H. Won, C.H. Choi, J. Chung, M.W. Chung, E.-H. Kim, S.I. Woo, Rational design of a hierarchical tin dendrite electrode for efficient electrochemical reduction of CO_2 , *ChemSusChem* 8 (2015) 3092.
- [24] W.Z. Zheng, Y. Wang, L. Shuai, X.Y. Wang, F. He, C.J. Lei, Z.J. Li, B. Yang, L.C. Lei, C. Yuan, M. Qiu, Y. Hou, X.L. Feng, Highly boosted reaction kinetics in carbon dioxide electroreduction by surface introduced electronegative dopants, *Adv. Funct. Mater.* 31 (2021) 2008146.

- [25] Y.Y. Cheng, J. Hou, P. Kang, Integrated capture and electroreduction of flue gas CO₂ to formate using amine functionalized SnO_x nanoparticles, *ACS Energy Lett.* 6 (2021) 3352–3358.
- [26] F.W. Li, S.-F. Zhao, L. Chen, A. Khan, D.R. MacFarlane, J. Zhang, Polyethylenimine promoted electrocatalytic reduction of CO₂ to CO in aqueous medium by graphene-supported amorphous molybdenum sulphide, *Energy Environ. Sci.* 9 (2016) 216–223.
- [27] F. Li, L. Chen, M. Xue, T. Williams, Y. Zhang, D.R. MacFarlane, J. Zhang, Towards a better Sn: efficient electrocatalytic reduction of CO₂ to formate by Sn/SnS₂ derived from SnS₂ nanosheets, *Nano Energy* 31 (2017) 270–277.
- [28] A. Zhang, R. He, H.P. Li, Y.J. Chen, T.Y. Kong, K. Li, H.X. Ju, J.F. Zhu, W.G. Zhu, J. Zeng, Nickel doping in atomically thin tin disulfide nanosheets enables highly efficient CO₂ reduction, *Angew. Chem. Int. Ed.* 57 (2018) 10954–10958.
- [29] J.S. Zou, C.-Y. Lee, G.G. Wallace, Boosting formate production from CO₂ at high current densities over a wide electrochemical potential window on a SnS catalyst, *Adv. Sci.* 8 (2021) 2004521.
- [30] X.L. Zheng, P.D. Luna, F.P. García de Arquer, B. Zhang, N. Becknell, M.B. Ross, Y. F. Li, M.N. Banis, Y.Z. Li, M. Liu, O. Voznyy, C.T. Dinh, T.T. Zhuang, P. Stadler, Y. Cui, X.W. Du, P.D. Yang, E.H. Sargent, Sulfur-modulated tin sites enable highly selective electrochemical reduction of CO₂ to formate, *Joule* 1 (2017) 794–805.
- [31] S. Gao, Y. Lin, X.C. Jiao, Y.F. Sun, Q.Q. Luo, W.H. Zhang, D.Q. Li, J.L. Yang, Y. Xie, Partially oxidized atomic cobalt layers for carbon dioxide electroreduction to liquid fuel, *Nature* 529 (2016) 68–71.
- [32] W. Zhang, J. Qi, K.Q. Liu, R. Cao, A nickel-based integrated electrode from an autologous growth strategy for highly efficient water oxidation, *Adv. Energy Mater.* 6 (2016) 1502489.
- [33] Y.G. Li, H.L. Wang, L.M. Xie, Y.Y. Liang, G.S. Hong, H.J. Dai, MoS₂ nanoparticles grown on graphene: An advanced catalyst for the hydrogen evolution reaction, *J. Am. Chem. Soc.* 133 (2011) 7296–7299.
- [34] M. Zhao, M.M. Liu, Y.Q. Dong, C. Zou, K.Q. Yang, Y. Yang, L.J. Zhang, S.M. Huang, Epitaxial growth of two-dimensional SnSe₂/MoS₂ misfit heterostructures, *J. Mater. Chem. C* 4 (2016) 10215–10222.
- [35] T. Kambe, R. Sakamoto, K. Hoshiko, K. Takada, M. Miyachi, J.-H. Ryu, S. Sasaki, J. Kim, K. Nakazato, M. Takata, H. Nishihara, π -conjugated nickel bis(dithiolene) complex nanosheet, *J. Am. Chem. Soc.* 135 (2013) 2462–2465.
- [36] D. Sheberla, L. Sun, M.A.B. Forsythe, S. Er, C.R. Wade, C.K. Brozek, A.A. Guzik, M. Dincă, High electrical conductivity in Ni₃(2,3,6,7,10,11-hexaiminotriphenylene)₂, a semiconducting metal-organic graphene analogue, *J. Am. Chem. Soc.* 136 (2014) 8859–8862.
- [37] S. Nakayama, T. Sugihara, J. Matsumoto, T. Notoya, T. Osakai, Chemical state analysis of tin oxide films by voltammetric reduction, *J. Electrochem. Soc.* 158 (2011) 341–345.
- [38] B. Kumar, V. Atla, J.P. Brian, S. Kumari, T.Q. Nguyen, M. Sunkara, J.M. Spurgeon, Reduced SnO₂ porous nanowires with a high density of grain boundaries as catalysts for efficient electrochemical CO₂-into-HCOOH conversion, *Angew. Chem. Int. Ed. Engl.* 56 (2017) 3645–3649.
- [39] S.B. Liu, X.F. Lu, J. Xiao, X. Wang, X.W. Lou, Bi₂O₃ nanosheets grown on multi-channel carbon matrix to catalyze efficient CO₂ electroreduction to HCOOH, *Angew. Chem. Int. Ed. Engl.* 58 (2019) 13828–13833.
- [40] Q.N. Wang, H. Dong, H. Yu, H.B. Yu, Enhanced performance of gas diffusion electrode for electrochemical reduction of carbon dioxide to formate by adding polytetrafluoroethylene into catalyst layer, *J. Power Sources* 279 (2015) 1–5.
- [41] C.C. Zhao, J.L. Wang, Electrochemical reduction of CO₂ to formate in aqueous solution using electro-deposited Sn catalysts, *Chem. Eng. J.* 293 (2016) 161–170.
- [42] Y. Zhao, J.J. Liang, C.Y. Wang, J.M. Ma, G.G. Wallace, Tunable and efficient tin modified nitrogen-doped carbon nanofibers for electrochemical reduction of aqueous carbon dioxide, *Adv. Energy Mater.* 8 (2018) 1702524.
- [43] D. Li, J. Wu, T.T. Liu, J. Liu, Z.Y. Yan, L. Zhen, Y.J. Feng, Tuning the pore structure of porous tin foam electrodes for enhanced electrochemical reduction of carbon dioxide to formate, *Chem. Eng. J.* 375 (2019) 122024.
- [44] W. Luc, C. Collins, S.W. Wang, H.L. Xin, K. He, Y.J. Kang, F. Jiao, Ag–Sn bimetallic catalyst with a core-shell structure for CO₂ reduction, *J. Am. Chem. Soc.* 139 (2017) 1885–1893.
- [45] S.Y. Choi, S.K. Jeong, H.J. Kim, Il-H. Baek, K.T. Park, Electrochemical reduction of carbon dioxide to formate on tin-lead alloys, *ACS Sustain. Chem. Eng.* 4 (2016) 1311–1318.
- [46] H.C. He, K. Liu, K.X. Liang, A. Mustapha, Z. Wang, L.L. Wu, C.C. Yang, L. Deng, S. J. Guo, Y.-N. Liu, Boosting carbon dioxide electroreduction to C₁ feedstocks via theory-guided tailoring oxygen defects in porous tin-oxide nanocubes, *J. Catal.* 385 (2020) 246–254.
- [47] J.H. Koh, D.H. Won, T. Eom, N.-K. Kim, K.D. Jung, H. Kim, Y.J. Hwang, B.K. Min, Facile CO₂ electro-reduction to formate via oxygen bidentate intermediate stabilized by high-index planes of Bi dendrite catalyst, *ACS Catal.* 7 (2017) 5071–5077.
- [48] C.W. Lee, J.S. Hong, K.D. Yang, K. Jin, J.H. Lee, H.-Y. Ahn, H. Seo, N.-E. Sung, K. T. Nam, Selective electrochemical production of formate from carbon dioxide with bismuth-based catalysts in an aqueous electrolyte, *ACS Catal.* 8 (2018) 931–937.
- [49] W.J. Zhang, Y. Hu, L.B. Ma, G.Y. Zhu, P.Y. Zhao, X.L. Xue, R.P. Chen, S.Y. Yang, J. Ma, J. Liu, Z. Jin, Liquid-phase exfoliated ultrathin Bi nanosheets: Uncovering the origins of enhanced electrocatalytic CO₂ reduction on two-dimensional metal nanostructure, *Nano Energy* 53 (2018) 808–816.
- [50] Z.M. Detweiler, J.L. White, S.L. Bernasek, A.B. Bocarsly, Anodized indium metal electrodes for enhanced carbon dioxide reduction in aqueous electrolyte, *Langmuir* 30 (2014) 7593–7600.
- [51] F.W. Li, M.Q. Xue, J.Z. Li, X.L. Ma, L. Chen, X.J. Zhang, D.R. MacFarlane, J. Zhang, Unlocking the electrocatalytic activity of antimony for CO₂ reduction by two-dimensional engineering of the bulk material, *Angew. Chem. Int. Ed. Engl.* 56 (2017) 14718–14722.
- [52] H.X. Wang, Y.B. Chen, X.L. Hou, C.Y. Ma, T.W. Tan, Nitrogen-doped graphenes as efficient electrocatalysts for the selective reduction of carbon dioxide to formate in aqueous solution, *Green Chem.* 18 (2016) 3250–3256.
- [53] H. Wang, J. Jia, P.F. Song, Q. Wang, D.B. Li, S.X. Min, C.X. Qian, L. Wang, Y.F. Li, C. Ma, T. Wu, J.Y. Yuan, M. Antonietti, G.A. Ozin, Efficient electrocatalytic reduction of CO₂ by nitrogen-doped nanoporous carbon/carbon nanotube membranes: A step towards the electrochemical CO₂ refinery, *Angew. Chem. Int. Ed. Engl.* 56 (2017) 7847–7852.
- [54] T.S. Perova, E. Kasper, M. Oehme, S. Cherevkov, J. Schulze, Features of polarized Raman spectra for homogeneous and non-homogeneous compressively strained Ge_{1-x}Sn_y alloys, *J. Raman Spectrosc.* 48 (2017) 993–1001.
- [55] T.-T. Zhuang, Z.-Q. Liang, A. Seifitokaldani, Y. Li, P.D. Luna, T. Burdyny, F.L. Che, F. Meng, Y.M. Min, R. Quintero-Bermudez, C.T. Dinh, Y.J. Pang, M. Zhong, B. Zhang, J. Li, P.-N. Chen, X.-L. Zheng, H.Y. Liang, W.-N. Ge, B.-J. Ye, D. Sinton, S.-H. Yu, E.H. Sargent, Steering post-C-C coupling selectivity enables high efficiency electroreduction of carbon dioxide to multi-carbon alcohols, *Nat. Catal.* 1 (2018) 421–428.
- [56] J. Li, G.X. Chen, Y.Y. Zhu, Z. Liang, A. Pei, C.-L. Wu, H.X. Wang, H.R. Lee, K. Liu, S. Chu, Y. Cui, Efficient electrocatalytic CO₂ reduction on a three-phase interface, *Nat. Catal.* 1 (2018) 592–600.
- [57] C.Y. Hu, Q.Y. Ma, S.-F. Hung, Z.-N. Chen, D.H. Ou, B. Ren, H.M. Chen, G. Fu, N. F. Zheng, In situ electrochemical production of ultrathin nickel nanosheets for hydrogen evolution electrocatalysis, *Chem* 3 (2017) 122–133.
- [58] H.-K. Lim, H. Shin, W.A. Goddard III, Y.J. Hwang, B.K. Min, H. Kim, Embedding covalency into metal catalysts for efficient electrochemical conversion of CO₂, *J. Am. Chem. Soc.* 136 (2014) 11355–11361.
- [59] A. Aljabour, H. Coskun, X.L. Zheng, M.G. Kibria, M. Strobel, S. Hild, M. Kehrler, D. Stifter, E.H. Sargent, P. Stadler, Active sulfur sites in semimetallic titanium disulfide enable CO₂ electroreduction, *ACS Catal.* 10 (2020) 66–72.